Dirac State in the FeB$_2$ Monolayer with Graphene-Like Boron Sheet

Haijun Zhang,[†,‡] Yafei Li,[§] Jianhou Hou,[†] Aijun Du,[‖] and Zhongfang Chen*,[†]

[†]Department of Chemistry, Institute for Functional Nanomaterials, University of Puerto Rico, Rio Piedras Campus, San Juan, Puerto Rico 00931, United States

[‡]School of Physics and Materials Science, Anhui University, Hefei 230601, China

[§]College of Chemistry and Materials Science, Jiangsu Key Laboratory of Biofunctional Materials, Nanjing Normal University, Nanjing, Jingsu 210023, China

[‖]School of Chemistry, Physics and Mechanical Engineering Faculty, Queensland University of Technology, Garden Point Campus, Brisbane, Queensland 4001, Australia

S Supporting Information

ABSTRACT: By introducing the commonly utilized Fe atoms into a two-dimensional (2D) honeycomb boron network, we theoretically designed a new Dirac material of FeB$_2$ monolayer with a Fermi velocity in the same order of graphene. The electron transfer from Fe atoms to B networks not only effectively stabilizes the FeB$_2$ networks but also leads to the strong interaction between the Fe and B atoms. The Dirac state in FeB$_2$ system primarily arises from the Fe d orbitals and hybridized orbital from Fe-d and B-p states. The newly predicted FeB$_2$ monolayer has excellent dynamic and thermal stabilities and is also the global minimum of 2D FeB$_2$ system, implying its experimental feasibility. Our results are beneficial to further uncovering the mechanism of the Dirac cones and providing a feasible strategy for Dirac materials design.
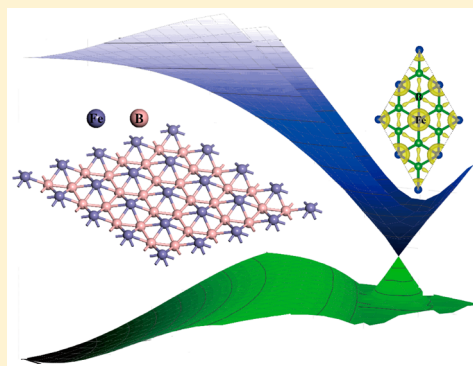
KEYWORDS: Dirac, fermion, FeB$_2$, density functional theory

Two-dimensional (2D) Dirac fermion systems,[1,2] as exemplified by graphene, have rather unique properties. The massless Fermions in graphene leads to half-integer/fractional/fractal quantum Hall effects,[3−9] ultrahigh carrier mobility,[10,11] and many other fascinating phenomena and properties.[12] The enthralling characteristics of Dirac cones in graphene promoted further exploration of other 2D materials with massless Dirac Fermions, such as the silicene and germanene,[13] graphynes,[14] $Pmmn$ and $P6/mmm$ boron,[15,16] as well as 2D topological insulators.[17] However, the poor variety is still challenging the experimental feasibility and practical applications of the Dirac materials. It is of great importance to theoretically or experimentally search for the Dirac materials beyond the carbonic and topological materials.

Due to the electron deficiency, the graphene-like hexagonal structure made of boron is not stable, and it is known that the boron sheets containing hexagon holes, namely the α-sheet and β-sheet, are energetically more favorable.[18−22] Note that in graphene each hexagon ring has two π electrons.[23] Thus, adding two electrons to each boron ring, for example, by embedding a metal atom which has a suitable size and can donate two electrons to the boron framework to achieve both the electronic and geometric fit,[24] we could get the isoelectronic analogue of graphene in the obtained metal-embedded hexagonal boron sheet. Though not explicitly mentioned, this strategy was used to design metal-boride monolayers, such as MgB$_2$,[25] BeB$_2$,[26] and TiB$_2$.[27] Interestingly,

the TiB$_2$ monolayer has Dirac states originated primarily from the d ortibals of Ti, but the freestanding TiB$_2$ exhibits a bending instability, the vertical distance between Ti and B layer is as far as 1.19 Å,[27] which could be understood by the large radius of Ti relative to the diameter of hexagonal boron ring. Recently, it has been found that Fe can well fit in the B$_6$H$_6$ unit to form a stable Fe©B$_6$H$_6$ cluster[28] with a unique chemical bonding pattern, namely planar hypercoordination.[29,30] A question raises naturally, is it possible to get an embedded hexagonal boron monolayer containing planar hypercoordinated metal and exhibiting Dirac states in the band structure?

In this work, by means of comprehensive density functional theory (DFT) computations, we designed a new Dirac material with a remarkable Fermi velocity (6.54×10^5 m/s), namely the FeB$_2$ monolayer, which contains the embedded planar hexacoordinate Fe atoms in the 2D honeycomb lattice or boron. The electron transfer from the Fe atoms to the honeycomb boron sheets effectively stabilizes the 2D boron networks, and results in the Dirac states in the band structure. This newly predicted monolayer has excellent dynamic and thermal stabilities, and is the global minimum of 2D FeB$_2$ system, all implying its experimental feasibility.

2. Computational Details. DFT computations used the projector augmented wave (PAW) approach[31,32] to represent the ion-electron interaction, as implemented in the Vienna ab initio simulation package (VASP).[33] The electron exchange-correlation functional was treated using generalized gradient approximation (GGA) in the form proposed by Perdew, Burke, and Ernzerhof (PBE).[34] The energy precision was set to 10^{-6} eV and atomic position was fully relaxed until the maximum force on each atom was less than 10^{-4} eV/Å. The 600 eV energy cutoff was adopted and Brillouin zone was sampled with a $11 \times 11 \times 1$ Γ-centered Monkhorst−Pack k-points grid for geometry optimization and self-consistent calculations.

The FeB_2 monolayer sheet was placed in x−y plane with the z direction perpendicular to the layer plane and a vacuum space of 15 Å in the z direction was used to avoid interactions between adjacent layers. Hexagonal MoS_2 (h-MoS_2) monolayer was employed as a representative substrate to verify the experimental feasibility and robust Dirac cone of FeB_2 monolayer. Phonon dispersion analysis was performed for 6 × 6 supercell (36 Fe atoms and 72 B atoms) using the Phonopy code[35] interfaced with the density functional perturbation theory (DFPT)[36] as implemented in VASP. The damped van der Waals (vdW) correction based on Grimme's scheme[37] was incorporated to describe the nonbonding interaction in geometry optimization of the FeB_2 bilayer and FeB_2/MoS_2 hybrid system. For strain-modified FeB_2 systems, the biaxial tensile or compressive strains were applied by fixing the lattice constant to a series of values, which are larger or smaller than that of equilibrium structure. The strain was defined as $\varepsilon = \Delta a/a_0$, where a_0 and $a = \Delta a + a_0$ are lattice constants of the unstrained and strained cell, respectively. According to the crystal symmetry, band structures of FeB_2 monolayer and FeB_2/MoS_2 hybrid sheet were calculated along the special lines connecting the following high-symmetry points, Γ (0, 0, 0), M (0.5, 0, 0), K (1/3, 1/3, 0), and Γ (0, 0, 0) in the k-space. To further confirm the Dirac states in FeB_2 monolayer, spin−orbit coupling (SOC) effect was included in electronic computation for one model. Moreover, Heyd−Scuseria−Ernzerhof (HSE06)[38] was used to calculate more reliable band structures and Fermi velocities. The 45 × 45 × 1 Monkhorst−Pack k-points grid was used to calculate the density of state (DOS) at the vicinity of Dirac point. A matrix k-points in $k_x k_y$ plane, including K (1/3, 1/3, 0) point, were used to calculate the eigenvalues at different k points and plot the 3D Dirac cone at K point.

The ab initio molecular dynamics (AIMD) simulations were also carried out to evaluate the thermal stabilities of FeB_2 monolayer. The initial configurations of FeB_2 monolayers with 4 × 4 supercell (16 Fe atoms and 32 B atoms) was annealed at different temperatures of 300 K, 500 K, 1000 K, 1500 K, and 2000 K. AIMD simulation in NVT ensemble lasts for 10 ps with a time step of 2.0 fs. The temperature was controlled by using the Nosé−Hoover method.[39]

The particle-swarm optimization (PSO) method within the evolutionary algorithm, as implemented in CALYPSO code,[40] was employed to search for the lowest-energy structures of 2D FeB_2 sheets. In our PSO calculations, the population size is set to 50, and the number of generation was maintained at 30. Unit cells containing total atoms of 3, 12, and 27 were considered.

3. Results and Discussion. *3.1. Geometric Structure and Thermodynamic Stability of FeB_2 Monolayer.* Figure 1 presents the top and side views of atomic structure for FeB_2 2D system, in which B atoms are arranged in a honeycomb
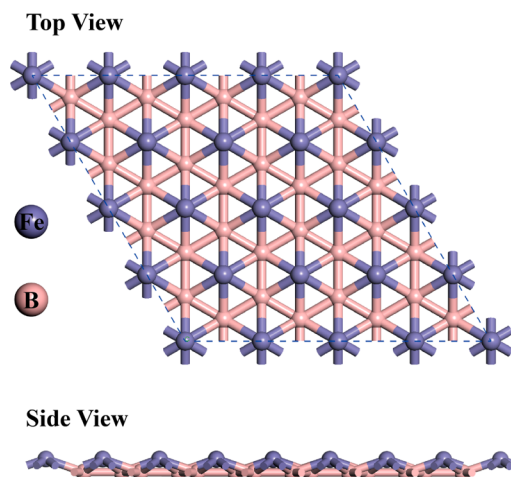

Figure 1. Optimized geometric structure the FeB_2 monolayer. The Fe atoms are located above the center of hexagonal boron rings.

lattice and Fe atoms are ca. 0.6 Å above the center of six-membered boron rings. This monolayer sheet can be considered as a one-layer Fe−B sheet exfoliated from bulk FeB_2 (P6/mmm) or graphene-like B sheet embedded by Fe atoms. In this quasi-planar FeB_2 sheet, each Fe atom coordinates with six boron atoms around it, thus forming planar hexacoordination. The B−B bond length (1.83 Å) is about the same as that in the bulk FeB_2 (1.76 Å)[41] but slightly larger than that in the B monolayers (1.67 Å ∼ 1.71 Å).[18−22] The length of Fe−B bond in FeB_2 monolayer (1.94 Å) is noticeably smaller than that in bulk FeB_2 crystal (2.32 Å), suggesting a much stronger interaction between the Fe atoms and boron layer.

To evaluate the relative stability of this FeB_2 monolayer sheet, we computed its cohesive energy $E_{coh} = (xE_{Fe} + 2xE_B - xE_{FeB_2})/3x$, where E_{Fe}, E_B, and E_{FeB_2} are the total energies of a single Fe atom, a single B atom, and one unit cell of the FeB_2 monolayer. The large cohesive energy (4.87 eV/atom) suggests that the FeB_2 monolayer is a strongly bonded network.

The stability of FeB_2 sheet can be further tested by carrying out the AIMD simulations at different temperatures. A relative large 4 × 4 supercell was used in the simulations at the temperatures of 500 K, 1000 K, 1500 K, and 2000 K. Snapshots of the geometries at the end of 10 ps simulations (Figure 2) show that the FeB_2 sheet can maintain its original configuration with hexacoordinated Fe atoms and graphene-like arranged boron sheet at the temperature up to 1000 K (the distorted structure can restore the planar structure after geometry optimization), but it will collapse at extremely high temperatures of 1500 and 2000 K. Especially, the hexacoordination of Fe obviously transfers to even higher (seven or eight) coordination at the temperature of 2000 K, which is in consistence with the results of our recent studies on the FeB_6 monolayers.[30e]

The well-preserved geometries of FeB_2 at the high temperatures of 1000 K indicate the promising thermal stability of this 2D FeB_2 system and its possible utilization at an extremely high temperature.

Additionally, to examine the dynamic stability, we computed the phonon dispersion of FeB_2 sheet along the high-symmetry lines in first Brillouin zone (Figure S1). There is no appreciable imaginary frequency in the phonon spectrum, implying the dynamic stability of this 2D FeB_2 system. Noteworthy, the
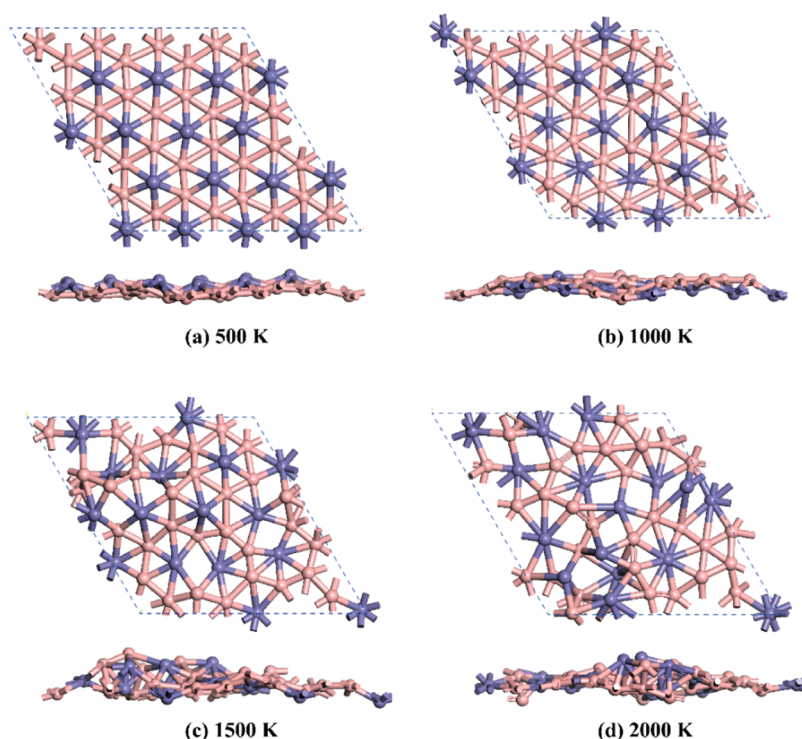
Figure 2. Snapshots for the equilibrium structures of FeB_2 monolayer at the temperatures of (a) 500 K, (b) 1000 K, (c) 1500 K, and (d) 2000 K, at the end of 10 ps AIMD simulations.
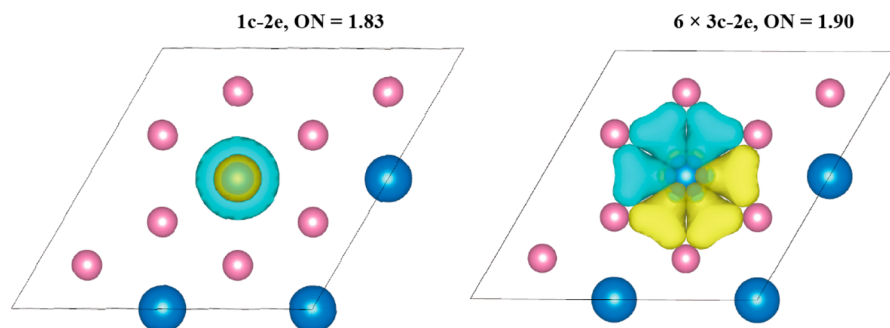

Figure 3. Schematic of SSAdNDP chemical bonding pattern for FeB_2 monolayer.

largest frequency in phonon spectrum of FeB_2, can reach up to 854 cm^{-1}, even greater than that in MoS_2 (473 cm^{-1}),[42] which also strongly suggests the robustness of Fe−B and B−B interactions in this novel FeB_2 monolayer.

3.2. Chemical Bonding and Stabilization Mechanism. What accounts for the high stabilities of FeB_2 monolayer as discussed above? For a deep insight of the bonding nature and stabilization mechanism, we first calculated the electron localization functions (ELF)[43] to analyze the electron distributions of this FeB_2 monolayer. ELF can be described in the form of a contour pot in real space with values ranging from 0 to 1. The region with 1 indicates the strong covalent electrons or lone-pair electrons, the region close to 0 implies the area with low electron density. In the meantime, the region with 0.5 is an area with homogeneous electron gas. As shown in Figure S2a, the electrons are mainly distributed and well delocalized at the region of boron network, which can electronically stabilize the 2D boron framework in the FeB_2 monolayer. To highlight the in-plane σ states, we also plot isosurface of ELFs for FeB_2 monolayer with an isovalue of 0.70 au (Figure S3). The ELF localization centers at the middle of

B−B bonds, denoting the strong covalent electron state with σ-like sp^2 hybridization like that in graphene. The σ bonds between the boron atoms can also be evidenced by the ELF map sliced perpendicular to (001) direction for FeB_2 monolayer (Figure S2b). Moreover, significant electron transfer from Fe to B atoms, as indicated by the different colored regions in the ELF map and by the Hirschfeld charge analysis (each Fe transfers 0.051*e* to B atoms while each B atom captures 0.026*e* from Fe atoms), leads to the electron supplement for boron frameworks and thus stabilizes the FeB_2 sheet.

We further examined the chemical bonding patterns of the 2D FeB_2 system by using the recently developed solid state adaptive natural density partitioning (SSAdNDP) method.[44] The SSAdNDP results suggest that besides the lone-pair electron on Fe atom, there are six three-center-two-electron (3c-2e) B−Fe−B bonds in one cell of FeB_2 monolayer (Figure 3). Accordingly, the abundance of multicenter bonds in FeB_2 monolayer leads to robust connection between the Fe and B atoms, and thus, the pronouncing stability of this 2D Fe−B network.

The FeB_6H_6 cluster (D_{6h}) can be viewed as the basic component of the FeB_2 monolayer. Note that in this cluster there is robust interaction between the peripheral boron ring and central Fe atom. Such a strong interaction is mainly attributed to two kind of molecular orbitals (MOs), namely the delocalized π MOs consisting of $3d_{xz}$, and $3d_{yz}$ orbitals of the Fe atom and $2p_z$ orbitals of the B atoms, and the remarkably delocalized σ MOs comprising of B $2p_x$ and $2p_y$ orbitals and Fe $3d_{xy}$ and $3d_{x^2-y^2}$ orbitals.[28] The good electronic and geometric fits between Fe atom and boron ring in FeB_6H_6 cluster is rather similar to the FeB_2 monolayer, which may also help us understand the high stability of the 2D FeB_2 system.

3.3. Band Structure and Dirac States in the FeB₂ Monolayer.

Then, we investigated the electronic properties, including the band structure and corresponding projected density of states (PDOS) of the FeB_2 monolayer (Figure 4).
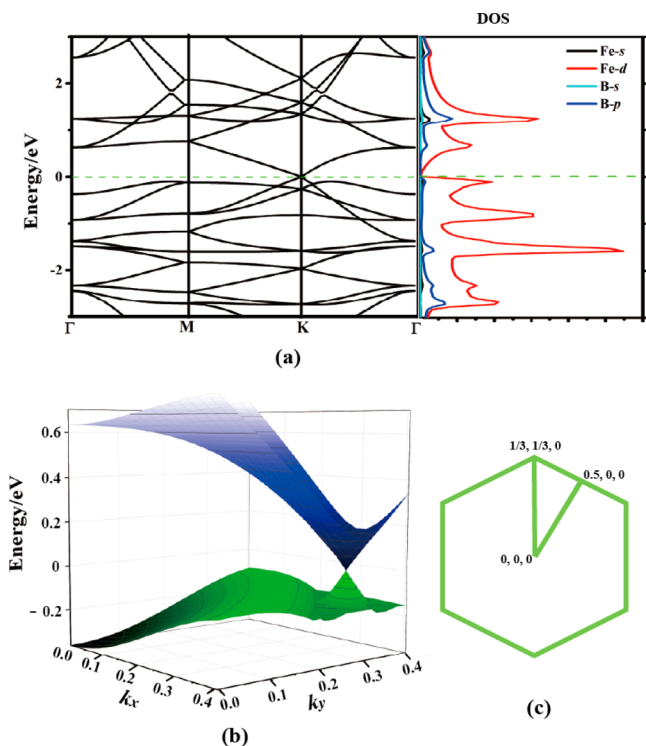

Figure 4. Electronic structure of FeB_2 monolayer. (a) Band structure and projected DOS, as well as (b) Dirac cone formed by the valence and conduction bands in the vicinity of Dirac point. (c) First Brillouin zone with the special k points.

Notably, there are two linear bands crossing at the Fermi level, which is located at the high-symmetry K $(1/3, 1/3, 0)$ point. The linear bands and degenerate state at K point denote the appearance of Dirac states in this FeB_2 sheet. The PDOS shows that the Dirac states near the Fermi level are predominantly composed of d orbitals from the Fe atoms. We also computed the three-dimensional (3D) valence and conduction bands at the vicinity of Dirac point (Figure 4b), which further confirms that the valence and conduction energy bands meet at Fermi level and confirms the features of a distorted Dirac cone in its first Brillouin zone. Considering the spin−orbit coupling (SOC) effect on the electronic structures, we checked the band structure by including the SOC effect, but no band gap exists (Figure S4a).

The linear dispersion of energy bands in both the k_x and k_y directions suggests the zero effective mass of the carriers near the Fermi level. To examine the carrier mobility around the Dirac cone, the Fermi velocity was evaluated by linear fitting the first derivatives of the band lines near the Dirac point with HSE06 functional (Figure S4b). The Fermi velocity can be calculated with the expression $\nu_F = E/(\hbar k)$, where the E/k is the slope of valence band (VB) or conduction band (CB) and the $\hbar$ is the reduced Planck's constant. As listed in Table S1, the Fermi velocity is direction-dependent and has the largest value of 6.54×10^5 m/s, which is in the same order of graphene (9.5×10^5 m/s).[45]

Amazingly, the linear band lines crossing the Fermi level at K point and the Dirac cones in FeB_2 monolayers persist at biaxial tensile or compressive strains between −6% and 3% (Figures S5 and S6), denoting its possible application at more complicated mechanical environments. Moreover, the band structure of the distorted FeB_2 sheet (after the 10 ps AIMD simulation at 300 K) well retains the Dirac cone (Figure S7), which suggests the robustness of the Dirac cone against certain structural deformation at room temperature.

In view of the great success in band structure engineering for graphene, the band gap opening of this FeB_2 Dirac system is an interesting issue. Thus, we computed the band structures of FeB_2 under uniaxial strain using the HSE06 method (Figure S8). Interestingly, the zero gap of FeB_2 system can be effectively opened by applying mild uniaxial strain (−5% to ∼5%) along both the x and y directions, which can be easily realized in the experiments. The tunable electronic structure of the FeB_2 sheet further suggests the potential application of this newly predicted 2D Dirac material in various technologies, such as the optoelectronics and microelectronics.

3.4. Origin of the Dirac Cone in FeB₂ Monolayer.

To better understand the physical origin of the Dirac cone, we computed the band decomposed charge density at Dirac point (Figure 5). The charge density distribution of the highest valence band is derived from the d states of Fe atoms (Figure 5a). Meanwhile, the hybrids of in-plane (p orbitals from B) states and out-of-plane (d orbitals from Fe) states between the sublattices of honeycomb B and triangular Fe are responsible for charge density distribution of the lowest conduction band at the Dirac point (Figure 5b). The top valence band around the Dirac cone is mainly contributed by d_{yz} and $d_{x^2-y^2}$ orbitals from Fe atoms, whereas the bottom of conduction band is predominantly composed of d_{xy} and d_{xz} orbitals from Fe atoms (Table S2). The p_x and p_y orbital of B atoms, which are hybridized with d orbitals from Fe atoms (Figure 5b), also contribute. Accordingly, the hybrids of in-plane (p_x and p_y orbitals from B atoms, as well as the d_{xy} and $d_{x^2-y^2}$ orbitals) and out-of-plane (d_{yz} and d_{xz} orbitals from Fe atoms) are the unique feature which may result in the emergence of Dirac cone in FeB_2 monolayer.

The FeB_2 monolayer has rather unique chemical bonding, namely planar hexacoordinated iron, and is confirmed to be a Dirac material with a Fermi velocity approaching to graphene. However, is it feasible for us to obtain it experimentally?

The pronounced dynamic and thermal stabilities of FeB_2 monolayer could only denote that it is a local minimum of 2D FeB_2 sheet. Note that the global minimum structure has higher possibility to be realized in experimental process. Is the above-mentioned FeB_2 monolayer the global minimum? Accordingly, we performed a global search for the lowest-energy structures of 2D FeB_2 by using the PSO method, which has proven a
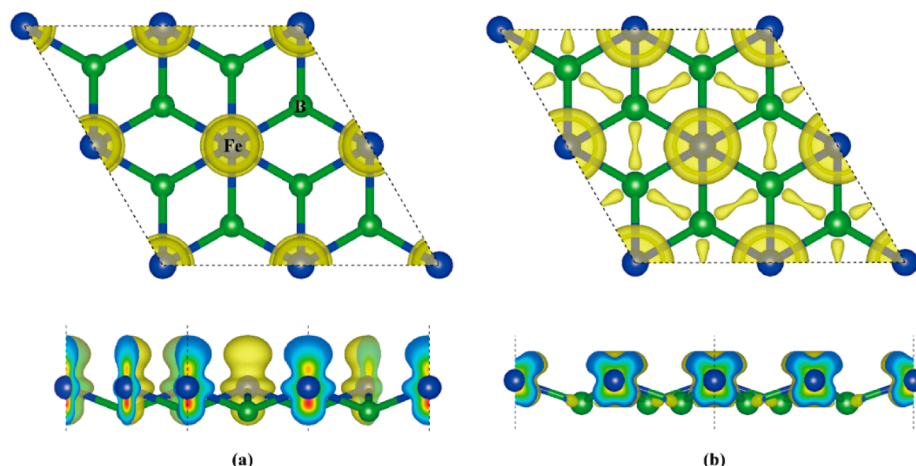
Figure 5. Band decomposed charge density of FeB_2 monolayer at Dirac point: projection of the charge density of (a) the highest valence band and (b) the lowest conduction band. The isosurface value was set at 0.005 au.

reliable strategy for globally searching the stable geometries of 2D structures.[30,40] Our global search led to two stable structures (Figure S9), our above-discussed FeB_2 is lower in energy by 143 meV/atom, thus is the global minimum structure in the 2D space.

As the global minimum in the 2D space, it holds a great promise to obtain FeB_2 monolayers experimentally. In view of the perfectly matched lattice constant between the MoS_2 monolayer ($a = 3.183$ Å) and the FeB_2 sheet ($a = 3.177$ Å), and the relatively weak van der Waals interaction between the two stacking layers as indicated by the computed interlay distances and binding energies within the FeB_2 bilayer and FeB_2/MoS_2 hybrid system (Figures S10 and S11 and Table S3), we propose to grow FeB_2 monolayer on the MoS_2 substrate or exfoliate FeB_2 single layer from the bulk FeB_2 ($P6/mmm$). Notably, the Dirac state can be remained in the FeB_2/MoS_2 hybrid system with AA stacking pattern, which demonstrates the feasibility of attaining Dirac states of FeB_2 sheet on an appropriate substrate (Figure S12).

4. Conclusion. To summarize, we successfully predicted a new Dirac material with a Fermi velocity approaching graphene, namely the hexagonal FeB_2 monolayer, which can be constructed by embedding the earth-abundant Fe into 2D graphene-like boron monolayer. The considerable electron transfer from Fe to B atoms stabilizes the otherwise electron deficient boron framework, and results in hybridization of Fe-d and B-p orbitals, which is the physical origin of the Dirac cone in this FeB_2 sheet. The Dirac cone persists at medium biaxial tensile or compressive strains (-6% to $\sim3\%$), but the zero gap of FeB_2 system can be effectively opened by applying mild uniaxial strain (-5% to $\sim5\%$). The newly predicted FeB_2 monolayer is the global minimum of 2D FeB_2 systems and has excellent thermal and kinetic stabilities, suggesting its experimental feasibility. We also propose to grow FeB_2 monolayer on the MoS_2 substrate or exfoliate FeB_2 single layer from the bulk FeB_2 ($P6/mmm$). With rather unique chemical bonding, namely planar hexacoordinate transition metal in the hexagonal boron network, and as an isoelectronic analogue of graphene, this experimentally highly feasible Dirac material has a high potential to be realized experimentally soon. We hope that the new design strategy presented here will also promote more theoretical and experimental efforts in developing 2D Dirac materials.

■ ASSOCIATED CONTENT

Ⓢ Supporting Information

The Supporting Information is available free of charge on the ACS Publications website at DOI: 10.1021/acs.nanolett.6b02335.

> Phonon dispersion spectrum of the FeB_2 monolayer; isosurfaces of ELF and ELF maps for FeB_2 monolayer plotted with the isovalue of 0.70 and 0.40 au; band structures of FeB_2 monolayer calculated by HSE06 method and by PBE functional including SOC effect; band structures of FeB_2 under different biaxial and uniaxial strains; geometry and band structure of FeB_2 monolayer after 10 ps AIMD simulation at 300 K; two different geometries of the 2D FeB_2 monolayer; geometries of the FeB_2 bilayer and FeB_2/MoS_2 coupling systems with different stacking geometries; band structure and PDOS of the FeB_2/MoS_2 coupling system; Fermi velocities along $\Gamma \rightarrow K$ and $M \rightarrow K$ direction; projected wave function character of the VBM and CBM at K (1/3, 1/3, 0) point; interlayer distances and binding energies of the bilayer FeB_2 sheets and FeB_2/MoS_2 coupling sheets. (PDF)

■ AUTHOR INFORMATION

Corresponding Author

*E-mail: zhongfangchen@gmail.com.

Notes

The authors declare no competing financial interest.

■ ACKNOWLEDGMENTS

■ REFERENCES

(1) Wehling, T.; Black-Schaffer, A. M.; Balatsky, A. V. *Adv. Phys.* **2014**, *63*, 1−76.

(2) Wang, J.; Deng, S.; Liu, Z.; Liu, Z. *Natl. Sci. Rev.* **2015**, *2*, 22.

(3) Novoselov, K.; Geim, A. K.; Morozov, S.; Jiang, D.; Katsnelson, M.; Grigorieva, I.; Dubonos, S.; Firsov, A. *Nature* **2005**, *438*, 197−200.

(4) Zhang, Y.; Tan, Y.-W.; Stormer, H. L.; Kim, P. *Nature* **2005**, *438*, 201−204.

(5) Bolotin, K. I.; Ghahari, F.; Shulman, M. D.; Stormer, H. L.; Kim, P. *Nature* **2009**, *462*, 196−199.

(6) Du, X.; Skachko, I.; Duerr, F.; Luican, A.; Andrei, E. Y. *Nature* **2009**, *462*, 192−195.

(7) Dean, C.; Wang, L.; Maher, P.; Forsythe, C.; Ghahari, F.; Gao, Y.; Katoch, J.; Ishigami, M.; Moon, P.; Koshino, M.; et al. *Nature* **2013**, *497*, 598−602.

(8) Ponomarenko, L.; Gorbachev, R.; Yu, G.; Elias, D.; Jalil, R.; Patel, A.; Mishchenko, A.; Mayorov, A.; Woods, C.; Wallbank, J.; et al. *Nature* **2013**, *497*, 594−597.

(9) Hunt, B.; Sanchez-Yamagishi, J.; Young, A.; Yankowitz, M.; LeRoy, B. J.; Watanabe, K.; Taniguchi, T.; Moon, P.; Koshino, M.; Jarillo-Herrero, P.; Ashoori, R. C. *Science* **2013**, *340*, 1427−1430.

(10) Bolotin, K. I.; Sikes, K.; Jiang, Z.; Klima, M.; Fudenberg, G.; Hone, J.; Kim, P.; Stormer, H. *Solid State Commun.* **2008**, *146*, 351−355.

(11) Hwang, E.; Sarma, S. D. *Phys. Rev. B: Condens. Matter Mater. Phys.* **2008**, *77*, 115449.

(12) Neto, A. C.; Guinea, F.; Peres, N.; Novoselov, K. S.; Geim, A. K. *Rev. Mod. Phys.* **2009**, *81*, 109.

(13) (a) Cahangirov, S.; Topsakal, M.; Aktürk, E.; Şahin, H.; Ciraci, S. *Phys. Rev. Lett.* **2009**, *102*, 236804. (b) Mannix, A. J.; Zhou, X. F.; Kiraly, B.; Wood, J. D.; Alducin, D.; Myers, B. D.; Liu, X.; Fisher, B. L.; Santiago, U.; Guest, J. R.; Yacaman, M. J.; Ponce, A.; Oganov, A. R.; Hersam, M. C.; Guisinger, N. P. *Science* **2015**, *350*, 1513−1516.

(14) Malko, D.; Neiss, C.; Viñes, F.; Görling, A. *Phys. Rev. Lett.* **2012**, *108*, 086804.

(15) Zhou, X.-F.; Dong, X.; Oganov, A. R.; Zhu, Q.; Tian, Y.; Wang, H.-T. *Phys. Rev. Lett.* **2014**, *112*, 085502.

(16) Ma, F.; Jiao, Y.; Gao, G.; Gu, Y.; Bilic, A.; Chen, Z.; Du, A. *Nano Lett.* **2016**, *16*, 3022−3028.

(17) Qi, X.-L.; Zhang, S.-C. *Rev. Mod. Phys.* **2011**, *83*, 1057.

(18) Tang, H.; Ismail-Beigi, S. *Phys. Rev. Lett.* **2007**, *99*, 115501.

(19) Galeev, T. R.; Chen, Q.; Guo, J.-C.; Bai, H.; Miao, C.-Q.; Lu, H.-G.; Sergeeva, A. P.; Li, S.-D.; Boldyrev, A. I. *Phys. Chem. Chem. Phys.* **2011**, *13*, 11575−11578.

(20) Wu, X.; Dai, J.; Zhao, Y.; Zhuo, Z.; Yang, J.; Zeng, X. C. *ACS Nano* **2012**, *6*, 7443−7453.

(21) Penev, E. S.; Bhowmick, S.; Sadrzadeh, A.; Yakobson, B. I. *Nano Lett.* **2012**, *12*, 2441−2445.

(22) Yu, X.; Li, L.; Xu, X.-W.; Tang, C.-C. *J. Phys. Chem. C* **2012**, *116*, 20075−20079.

(23) Popov, I. A.; Bozhenko, K. V.; Boldyrev, A. I. *Nano Res.* **2012**, *5*, 117−123.

(24) von Ragué Schleyer, P.; Boldyrev, A. I. *J. Chem. Soc., Chem. Commun.* **1991**, 1536−1538.

(25) Tang, H.; Ismail-Beigi, S. *Phys. Rev. B: Condens. Matter Mater. Phys.* **2009**, *80*, 134113.

(26) Zhang, P.; Crespi, V. H. *Phys. Rev. Lett.* **2002**, *89*, 056403.

(27) Zhang, L.; Wang, Z.; Du, S.; Gao, H.-J.; Liu, F. *Phys. Rev. B: Condens. Matter Mater. Phys.* **2014**, *90*, 161402.

(28) Hou, J.; Duan, Q.; Qin, J.; Shen, X.; Zhao, J.; Liang, Q.; Jiang, D.; Gao, S. *Phys. Chem. Chem. Phys.* **2015**, *17*, 9644−9650.

(29) Romanescu, C.; Galeev, T. R.; Li, W.-L.; Boldyrev, A. I.; Wang, L.-S. *Acc. Chem. Res.* **2013**, *46*, 350−358.

(30) (a) Yang, L. M.; Ganz, E.; Chen, Z.; Wang, Z. X.; Schleyer, P. v. R. *Angew. Chem., Int. Ed.* **2015**, *54*, 9468−9501. (b) Yang, L. M.; Popov, I. A.; Frauenheim, T.; Boldyrev, A. I.; Heine, T.; Bačić, V.; Ganz, E. *Phys. Chem. Chem. Phys.* **2015**, *17*, 26043−26048. (c) Yang, L. M.; Popov, I. A.; Boldyrev, A. I.; Heine, T.; Frauenheim, T.; Ganz, E. *Phys. Chem. Chem. Phys.* **2015**, *17*, 17545−17551. (d) Yang, L. M.; Bačić, V.; Popov, I. A.; Boldyrev, A. I.; Heine, T.; Frauenheim, T.; Ganz, E. *J. Am. Chem. Soc.* **2015**, *137*, 2757−2762. (e) Zhang, H. J.; Li, Y. F.; Hou, J. H.; Tu, K. X.; Chen, Z. *J. Am. Chem. Soc.* **2016**, *138*, 5644−5651.

(31) Blöchl, P. E. *Phys. Rev. B: Condens. Matter Mater. Phys.* **1994**, *50*, 17953.

(32) Kresse, G.; Joubert, D. *Phys. Rev. B: Condens. Matter Mater. Phys.* **1999**, *59*, 1758.

(33) Kresse, G.; Hafner, J. *Phys. Rev. B: Condens. Matter Mater. Phys.* **1993**, *47*, 558.

(34) Perdew, J. P.; Burke, K.; Ernzerhof, M. *Phys. Rev. Lett.* **1996**, *77*, 3865.

(35) Togo, A.; Oba, F.; Tanaka, I. *Phys. Rev. B: Condens. Matter Mater. Phys.* **2008**, *78*, 134106.

(36) Baroni, S.; De Gironcoli, S.; Dal Corso, A.; Giannozzi, P. *Rev. Mod. Phys.* **2001**, *73*, 515.

(37) Grimme, S. *J. Comput. Chem.* **2006**, *27*, 1787−1799.

(38) Heyd, J.; Scuseria, G. E.; Ernzerhof, M. *J. Chem. Phys.* **2003**, *118*, 8207−8215.

(39) Martyna, G. J.; Klein, M. L.; Tuckerman, M. *J. Chem. Phys.* **1992**, *97*, 2635−2643.

(40) Wang, Y.; Lv, J.; Zhu, L.; Ma, Y. *Phys. Rev. B: Condens. Matter Mater. Phys.* **2010**, *82*, 094116.

(41) Voroshnin, L.; Lyakhovich, L.; Panich, G.; Protasevich, G. *Met. Sci. Heat Treat.* **1970**, *12*, 732−735.

(42) Molina-Sanchez, A.; Wirtz, L. *Phys. Rev. B: Condens. Matter Mater. Phys.* **2011**, *84*, 155413.

(43) Savin, A.; Nesper, R.; Wengert, S.; Fässler, T. F. *Angew. Chem., Int. Ed. Engl.* **1997**, *36*, 1808−1832.

(44) Galeev, T. R.; Dunnington, B. D.; Schmidt, J. R.; Boldyrev, A. I. *Phys. Chem. Chem. Phys.* **2013**, *15*, 5022−5029.

(45) Trevisanutto, P. E.; Giorgetti, C.; Reining, L.; Ladisa, M.; Olevano, V. *Phys. Rev. Lett.* **2008**, *101*, 226405.